Numerical simulation of breakup of a viscous drop in simple shear flow through a volume-of-fluid method

Jie Li, Yuriko Y. Renardy, and Michael Renardy

Citation: Physics of Fluids (1994-present) **12**, 269 (2000); doi: 10.1063/1.870305
View online: http://dx.doi.org/10.1063/1.870305
View Table of Contents: http://scitation.aip.org/content/aip/journal/pof2/12/2?ver=pdfcov
Published by the AIP Publishing

Numerical simulation of breakup of a viscous drop in simple shear flow through a volume-of-fluid method

Jie Li, Yuriko Y. Renardy,[a] and Michael Renardy
Department of Mathematics and ICAM, 460 McBryde Hall, Virginia Tech, Blacksburg, Virginia 24061-0123

(Received 10 March 1999; accepted 28 October 1999)

A spherical drop, placed in a second liquid of the same density, is subjected to shearing between parallel plates. The subsequent flow is investigated numerically with a volume-of-fluid (VOF) method. The scheme incorporates a semi-implicit Stokes solver to enable computations at low Reynolds number. Our simulations compare well with previous theoretical, numerical, and experimental results. For capillary numbers greater than the critical value, the drop deforms to a dumbbell shape and daughter drops detach via an end-pinching mechanism. The number of daughter drops increases with the capillary number. The breakup can also be initiated by increasing the Reynolds number. © *2000 American Institute of Physics.* [S1070-6631(00)02002-X]

I. INTRODUCTION

The study of dynamics of a drop in shear flow is of fundamental importance in dispersion science, and has evoked great interest, most notably since the experiments of G. I. Taylor.[1,2] The reader is referred to two review articles[3,4] for references on this subject. More recently, experimental observations of the sheared breakup have been recorded in Ref. 5: A strong shear is applied to a single drop, which elongates and undergoes end pinching via a process which is termed ''elongative end pinching'' as opposed to ''retractive end pinching,'' studied in Ref. 6. These processes, which yield daughter drops, are paradigms of theoretical investigations into emulsification and mixing.[4,7–9] Computational studies[10] have elucidated regimes where the drop deforms to the point of breaking, but results on the motion past breakup are limited. Further numerical exploration on the stages in the formation of daughter drops under shear are reported in this paper. The simulations are conducted as three-dimensional initial value problems, with the volume-of-fluid scheme.[11,12]

The experimental work of Ref. 5 focuses on a viscous drop suspended in a second immiscible liquid (the matrix liquid) in a cylindrical Couette device. The difference in density between the two liquids is a minor effect, and the flow is sufficiently slow, so that centrifugal effects in the cylindrical device are not important. A theoretical model for this is simply three-dimensional Couette flow with zero gravity, as shown in Fig. 1. The liquid drop has an undeformed radius a and viscosity μ_d, and the matrix liquid has viscosity μ_m. The matrix liquid is undergoing a simple shear flow between two parallel plates, placed a distance d^* apart. The undisturbed velocity field is $\mathbf{u}=\dot{\gamma}z\mathbf{i}$, where $\dot{\gamma}$ is the imposed shear rate. Additional parameters for our numerical simulations are the interfacial tension σ, and the spatial periodicities λ_x^* and λ_y^* in the x and y directions, respectively. There are six dimensionless parameters: A capillary number $\mathrm{Ca}=a\dot{\gamma}\mu_m/\sigma$, where an average shear rate is defined $\dot{\gamma}=U^*/d^*$, the viscosity ratio $\lambda=\mu_d/\mu_m$, the Reynolds number $\mathrm{Re}=\rho_m\dot{\gamma}a^2/\mu_m$, the dimensionless plate separation $d=d^*/a$, dimensionless spatial periodicities $\lambda_x=\lambda_x^*/a$ and $\lambda_y=\lambda_y^*/a$.

In the study of drop dynamics in shear flow, one of the greatest difficulties is that the domain of interest contains an unknown free boundary, namely the interface. The interface moves from one location to another, and may undergo severe deformations including breakup. The interface plays a major role in defining the system and it must be determined as part of the solution. To investigate this problem numerically, the primary step is to choose an interface tracking method.

There are many interface tracking methods,[13] such as the moving grid method, the front tracking method, the level set method and the volume-of-fluid method, hereinafter called the VOF method. Each of these methods has its own advantages and disadvantages. In the past, all numerical studies of a viscous drop in shear flow have been performed with the boundary integral method, combined with a front tracking method. An advantage of the front tracking method is the use of marker particles to track the interface explicitly; the information regarding location and curvature of the interface is explicitly available during the whole calculation process. Therefore, each boundary condition can be applied directly and accurately. This generally reduces by a considerable amount the resolution required to maintain accuracy. As a consequence, boundary integral methods have been applied successfully to the problem of drop deformation in shear flow. However, the implementation of boundary integral methods poses a major obstacle, because it is very difficult to handle merging and folding interfaces. This requires reordering the interface points and can result in a significant logical programming and computational overhead. The VOF method, on the other hand, provides a simple way of treating the topological changes of the interface, as well as ease of generalization to the three-dimensional case. The latter two issues are key issues in the simulation of drop breakup in simple shear flow. The VOF method was first introduced by DeBar[14] in 1974, followed by significant advance from

[a]Electronic mail: renardyy@math.vt.edu

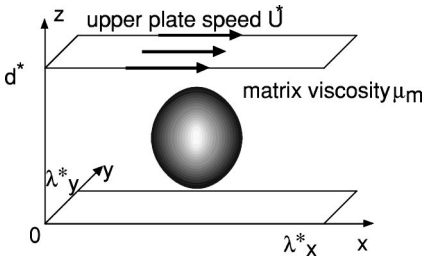

FIG. 1. Flow schematics. The computational domain is spatially periodic in the x and y directions with periodicities λ_x^* and λ_y^*, respectively. Plate separation is d^*. Upper wall moves with velocity $(U^*,0,0)$. The lower wall is at rest. Drop radius is a, and drop viscosity is μ_d. The matrix viscosity if μ_m.

Youngs' work[15] eight years later. Recent works include Refs. 16–19.

Our numerical study differs from previous works in the following points. The velocity and pressure are used as primitive variables and the incompressibility constraint is satisfied on the fluids by a projection method. The boundary integral method incorporates a simple shear flow out to infinity. We examine the limitations of this assumption by changing the plate separation, from placing the plates close to the drop and then farther away. We can also take into account the inertia term and consider higher Reynolds number flow, and therefore, investigate the approximation of low Reynolds number motion by Stokes flow. Previous numerical works, on the other hand, are quasi-steady Stokes flows: Given the drop shape at each time step, the boundary integral method is used to solve for a steady velocity field through an iteration. Our numerical method is designed to solve initial value problems, and a steady solution would be reached eventually. However, for capillary numbers close to critical, this evolution takes a longer time and becomes computationally expensive. From the theoretical point of view, our code could be converted to a steady code by neglecting the time-dependent acceleration term. However, the details in our projection method are not easily converted, and the numerical resolution does not become cheaper. We, therefore, compare the past Stokes flow results against low Reynolds number flow and against unsteady Stokes flow, where the inertial convective term has been neglected.

The VOF method conserves mass accurately, and this is essential for calculating the steady solution at low capillary numbers because the final shapes are obviously sensitive to the drop volume. However, questions have been raised on the accuracy of calculation for the surface tension force.[20] The goal of this work is, therefore, twofold. On the one hand, we investigate the physics of the deformation of a viscous drop by simple shear by the VOF method. On the other hand, this is a prototype problem to test the accuracy of the VOF method, through the comparison with existing results from the boundary integral approach. A satisfactory comparison will be shown in subsequent sections, thus justifying the use of the VOF method to explore the dynamics of a drop in the breakup regime, which is difficult to treat with the boundary integral method. The rest of this paper is organized as follows. In Sec. II, the governing equations and the numerical method are given. In Sec. III, we study the deformation of a viscous drop for subcritical capillary number, where the drop is stretched to an approximately ellipsoidal shape. The details of the shape and the values of the critical capillary number, computed by our method for various viscosity ratios of the drop to matrix liquids, agree quantitatively with results in the literature. The main advantage of our method is that it conserves mass, and no rescaling of the mass is needed during the calculation. A loss of mass would otherwise cause an overestimation of the interfacial tension force. This accuracy is especially important for the computation of this evolution, where each stage depends sensitively on the interfacial tension force. In Sec. IV, the breakup of a viscous drop is investigated. Figure 13 shows an experimental observation of Ref. 5 for two fluids of different viscosities, and our numerical simulation of Fig. 16 captures the main features. Initially, the elongative end-pinching mechanism produces the largest daughter drops, followed by the production of a small drop, then a large drop, then a small drop, then two large drops, toward the center of the bridge. Section V is an investigation of inertial effects. The dynamics of the drop breakup for Stokes flow is replicated at low Reynolds numbers, and the addition of a small amount of inertia leads to small changes. However, an increase in Reynolds number, which is equivalent to making the liquids less viscous, leads to more complicated flow patterns. Finally, a conclusion is given in Sec. VI.

II. NUMERICAL METHOD

A. The equations of motion

The flow is composed of two immiscible liquids of different densities and viscosities. The placement of the two fluids is represented by a concentration function C

$$C(\mathbf{x})=\begin{cases}1 & \text{fluid } 1\\ 0 & \text{fluid } 2\end{cases}. \tag{2.1}$$

The average values of density and viscosity are interpolated by the following formulas

$$\rho=C\rho_1+(1-C)\rho_2, \tag{2.2}$$

$$\mu=C\mu_1+(1-C)\mu_2. \tag{2.3}$$

The concentration function C is governed by a transport equation

$$\frac{\partial C}{\partial t}+\mathbf{u}\cdot\nabla C=0, \tag{2.4}$$

where $\mathbf{u}$ is the velocity of the flow. The fluids are incompressible

$$\nabla\cdot\mathbf{u}=0, \tag{2.5}$$

and governed by the Navier–Stokes equations

$$\rho\left(\frac{\partial\mathbf{u}}{\partial t}+\mathbf{u}\cdot\nabla\mathbf{u}\right)=-\nabla p+\nabla\cdot\mu\mathbf{S}+\mathbf{F}, \tag{2.6}$$

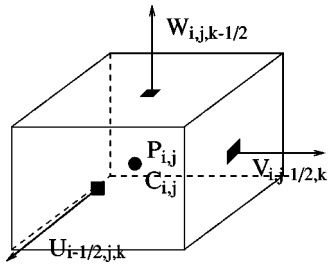

FIG. 2. Location of variables in a MAC mesh cell.

where ρ is the density, μ the viscosity, p the pressure, $\mathbf{S}$ the strain rate tensor

$$\mathbf{S}_{ij}=\frac{1}{2}\left(\frac{\partial u_j}{\partial x_i}+\frac{\partial u_i}{\partial x_j}\right),$$

and $\mathbf{F}$ the source term for the momentum equation. $\mathbf{F}$ includes gravity and the interfacial tension force. The interfacial tension force is $\mathbf{F}_s=\sigma\kappa\mathbf{n}_S\delta_s$, where σ is the interfacial tension, κ is the mean curvature and $\mathbf{n}_S$ is the normal to the interface.

B. Temporal discretization and projection method

Our numerical method is composed of three parts: A second-order VOF method to track the interface, a projection method to solve the Navier–Stokes equations on the MAC grid (Fig. 2), and finally, a continuum method for modeling the interfacial tension.[16,17,21–23] The 2D (two-dimensional) version is explained in detail in Ref. 11, and the axisymmetric version in Ref. 12. The generalization to the three-dimensional version is straightforward and we sketch it here.

1. The volume fraction field

In order to successfully represent and track the interface, we must answer three questions: (1) How do we represent the interface on a finite mesh? (2) How will the interface evolve in time? and (3) how should we apply boundary conditions on the interface? At the discrete level, the concentration function C is represented by the volume fraction of one fluid, say fluid 1. This is also called the VOF function. When a cell is filled by fluid 1, VOF=1, and when a cell does not contain any of this fluid, VOF=0. The interface lies in the cells with the VOF between 0 and 1. It is well known that the VOF method conserves mass while still maintaining a sharp representation of the interface. One of the most important ingredients is the accurate computation of the curvature of the interface from the volume fraction field. This difficulty provides a test of accuracy for our implementation of the boundary conditions posed at the interface.

Given an interface, we can calculate a unique volume fraction field. On the other hand, given a volume fraction field, the reconstruction of the interface, together with an accurate orientation and local curvature, poses a problem. This affects the approximation of the boundary conditions at the interface. The interfacial tension condition at the interface cannot be applied directly, but rather as a body force over the cells which contain the interface. Two such formulations have been implemented in this work. The first is the continuous surface force formulation of Ref. 24, in which $\mathbf{f}_s=\sigma\kappa\mathbf{n}_S$, and $\mathbf{F}_s=\mathbf{f}_s\nabla C$. The second is the formulation of Ref. 21, in which $\mathbf{F}_s=\nabla\cdot\mathbf{T}=\sigma\delta_S\kappa\mathbf{n}_S$ and $\mathbf{T}=[(\mathbf{1}-\mathbf{n}_S\otimes\mathbf{n}_S)\sigma\delta_S]$, which leads to a conservative scheme for the momentum equation. We have compared the results obtained from these two formulations. The difference is very small, roughly 1% for the simulation of a drop settling to a steady solution on the 64×64 mesh. We have a preference for the second formulation because we only need to estimate the first derivatives of $\mathbf{n}$.

2. The projection method

The simultaneous solution of the continuity and momentum equations is computationally expensive. An efficient approximation is provided by a projection method,[25] which proceeds as follows. Given the physical quantities at time level n, the first step is to calculate an intermediate velocity $\mathbf{u}^*$ which satisfies

$$\frac{\mathbf{u}^*-\mathbf{u}^n}{\Delta t}=-\mathbf{u}^n\cdot\nabla\mathbf{u}^n+\frac{1}{\rho}(\nabla\cdot(\mu\mathbf{S})+\mathbf{F})^n. \tag{2.7}$$

$\mathbf{u}^*$ is not, in general, divergence-free. We then correct $\mathbf{u}^*$ by the pressure term

$$\frac{\mathbf{u}^{n+1}-\mathbf{u}^*}{\Delta t}=-\frac{\nabla p}{\rho}, \tag{2.8}$$

where $\mathbf{u}^{n+1}$ at time level $n+1$ satisfies

$$\nabla\cdot\mathbf{u}^{n+1}=0. \tag{2.9}$$

The key idea of this projection method is to substitute Eq. (2.8) into Eq. (2.9), to obtain a Poisson equation for the pressure

$$\nabla\cdot\left(\frac{\nabla p}{\rho}\right)=-\frac{\nabla\cdot\mathbf{u}^*}{\Delta t}. \tag{2.10}$$

The solution of this equation is the most time-consuming part of the Navier–Stokes solver and an efficient solution is crucial for the performance of the whole method. Potentially, the multigrid method is the most efficient method. The basic idea of the multigrid method[26] is to combine two complementary procedures: One basic iterative method to reduce the high-frequency error, and one coarse grid correction step to eliminate the low-frequency error. We choose a two-color Gauss–Seidel iterative method because it breaks the dependence between the variables and, therefore, allows for parallelization of the scheme. We use a Garlerkin method to provide a good coarse grid correction.

3. Three-dimensional semi-implicit scheme

The above description completes the characterization of our numerical method. However, one weakness is that it is an explicit method, and not suitable for simulations of low Reynolds number flows or Stokes flows. For an explicit method, the time step Δt should be less than the viscous time scale, $T_\mu=\rho h^2/\mu$, where h denotes the mesh size. There-

fore, simulations of low Reynolds number flows or Stokes flows are subject to strict stability limitations and are expensive. In order to overcome this difficulty, we have presented a semi-implicit scheme for the two-dimensional case in Ref. 11 and proved that this scheme is unconditionally stable. It is more difficult to prove the stability of the three-dimensional (3D) scheme. The stability analysis can be carried out as follows. The 3D semi-implicit scheme for the u-component is

$$\frac{u^*-u^n}{\Delta t}=\frac{1}{\rho^n}\frac{\partial}{\partial x}(2\mu^n u_x^*)+\frac{1}{\rho^n}\frac{\partial}{\partial y}(\mu^n u_y^*+\mu^n v_x^n)+\frac{1}{\rho^n}\frac{\partial}{\partial z}(\mu^n u_z^*+\mu^n w_x^n), \tag{2.11}$$

and similarly for the v, w components. Let $u,v,w \sim \exp(i\alpha x+i\beta y+i\gamma z)$ and let $\mu=1$, $\rho=1$ for simplicity. Then

$$\begin{pmatrix} \frac{u^*-u^n}{\Delta t} \\ \frac{v^*-v^n}{\Delta t} \\ \frac{v^*-v^n}{\Delta t} \end{pmatrix} = \begin{pmatrix} -2\alpha^2-\beta^2-\gamma^2 & 0 & 0 \\ 0 & -\alpha^2-2\beta^2-\gamma^2 & 0 \\ 0 & 0 & -\alpha^2-\beta^2-2\gamma^2 \end{pmatrix} \begin{pmatrix} u^* \\ v^* \\ w^* \end{pmatrix} + \begin{pmatrix} 0 & -\alpha\beta & -\alpha\gamma \\ -\alpha\beta & 0 & -\beta\gamma \\ -\alpha\gamma & -\beta\gamma & 0 \end{pmatrix} \begin{pmatrix} u^n \\ v^n \\ w^n \end{pmatrix}, \tag{2.12}$$

which reduces to

$$\begin{pmatrix} 1+\Delta t(2\alpha^2+\beta^2+\gamma^2) & 0 & 0 \\ 0 & 1+\Delta t(\alpha^2+2\beta^2+\gamma^2) & 0 \\ 0 & 0 & 1+\Delta t(\alpha^2+\beta^2+2\gamma^2) \end{pmatrix} \begin{pmatrix} u^* \\ v^* \\ w^* \end{pmatrix} = \begin{pmatrix} 1 & -\alpha\beta\Delta t & -\alpha\gamma\Delta t \\ -\alpha\beta\Delta t & 1 & -\beta\gamma\Delta t \\ -\alpha\gamma\Delta t & -\beta\gamma\Delta t & 1 \end{pmatrix} \begin{pmatrix} u^n \\ v^n \\ w^n \end{pmatrix}. \tag{2.13}$$

The eigenvalues of the left matrix are $1+\Delta t(2\alpha^2+\beta^2+\gamma^2)$, $1+\Delta t(\alpha^2+2\beta^2+\gamma^2)$ and $1+\Delta t(\alpha^2+\beta^2+2\gamma^2)$. The eigenvalues of the right matrix are solutions of the following *cubic* equation

$$\det\begin{pmatrix} 1-\lambda & -\alpha\beta\Delta t & -\alpha\gamma\Delta t \\ -\alpha\beta\Delta t & 1-\lambda & -\beta\gamma\Delta t \\ -\alpha\gamma\Delta t & -\beta\gamma\Delta t & 1-\lambda \end{pmatrix}=0. \tag{2.14}$$

Let $\eta=1-\lambda$. The above equation can be written as

$$\eta^3-(\alpha^2\beta^2+\alpha^2\gamma^2+\beta^2\gamma^2)\Delta t^2-2\alpha^2\beta^2\gamma^2\Delta t^3=0. \tag{2.15}$$

For the cubic equation

$$\eta^3+a\eta^2+b\eta+c=0, \tag{2.16}$$

we first compute

$$Q\equiv\frac{a^2-3b}{9}=\frac{1}{3}(\alpha^2\beta^2+\alpha^2\gamma^2+\beta^2\gamma^2)\Delta t^2,$$

$$R\equiv\frac{2a^3-9ab-27c}{54}=\alpha^2\beta^2\gamma^2\Delta t^3.$$

Since $Q^3\geqslant R^2$, the cubic equation has three real roots. These are found by computing

$$\theta=\arccos(R/\sqrt{Q^3}),$$

in terms of which the three roots are

$$\eta_1=-2\sqrt{Q}\cos\left(\frac{\theta}{3}\right)-\frac{a}{3},$$

$$\eta_2=-2\sqrt{Q}\cos\left(\frac{\theta+\pi}{3}\right)-\frac{a}{3}, \tag{2.17}$$

$$\eta_3=-2\sqrt{Q}\cos\left(\frac{\theta+2\pi}{3}\right)-\frac{a}{3}.$$

However,

$$|\eta_{1,2,3}|^2\leqslant(|2\sqrt{Q}|)^2\leqslant\tfrac{4}{3}(\alpha^2\beta^2+\alpha^2\gamma^2+\beta^2\gamma^2)\Delta t^2 \leqslant(\alpha^2+\beta^2+\gamma^2)^2\Delta t^2.$$

It is then easy to see the absolute values of the three eigenvalues of the right matrix are less than those of the left matrix. In summary, the above semi-implicit scheme is first-order accurate in time and unconditionally stable. The stability of this scheme is crucial for the simulation of low Reynolds number flow and Stokes flow.

C. Spatial discretization

An Eulerian mesh of rectangular cells is used. The momentum equations are finite differenced on a locally variable, staggered mesh. As Fig. 2 shows, the x component of veloc-

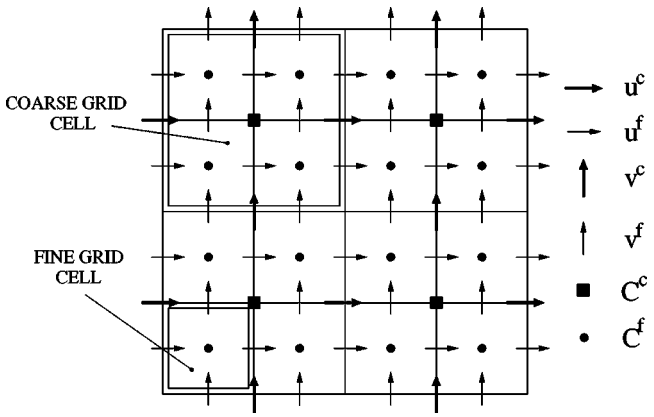

FIG. 3. Coarse and fine mesh grid.

ity $u_{i-(1/2),j,k}$, the y component of velocity $v_{i,j-(1/2),k}$ and the z component of velocity $w_{i,j,k-(1/2)}$ are centered at the right face, front face and top face of the cell, respectively, whereas the pressure, $p_{i,j,k}$ is located at the center. This is the so-called MAC method. In our previous work, the concentration function was defined on the same mesh grid as the velocity and the pressure. This is not obligatory. Indeed, low Reynolds number flow is characterized by slow change of velocity in space and in time. On the other hand, the flow behavior is dominated by the interface evolution. Therefore, in order to achieve accurate representation of the interface, more concentration values are needed. Based on this observation, we define the concentration function on a computational grid which is twice as fine as the grid for the velocity and pressure (Fig. 3). An adaptive mesh would be superior, but our two-level method is easily built upon our previous work and presents a compromise between the simplicity and the efficiency. To insert our previous routines into the two-level-mesh grid method, the only work we need to do is to implement a prolongation procedure, which extrapolates the velocities from the coarse grid to the fine grid and a restriction procedure, which transfers the concentration value from the fine grid to the coarse grid. The prolongation relations are derived by a bilinear interpolation. For each coarse grid node, four (eight) fine grid values are derived for the 2D case (3D case). For the u-velocity in the 2D case, let (ic,jc) and (if,jf) denote coarse and fine mesh indices, respectively. Then $if=2(ic)-1$, $jf=2(jc)-1$ and

$$
\begin{aligned}
&U^f(if,jf)=\tfrac{1}{4}(3U_1^c+U_2^c),\\
&U^f(if,jf+1)=\tfrac{1}{4}(U_1^c+3U_2^c),
\end{aligned}
\tag{2.18}
$$

$$
\begin{aligned}
&U^f(if+1,jf)=\tfrac{1}{8}(3U_1^c+U_2^c+3U_3^c+U_4^c),\\
&U^f(if+1,jf+1)=\tfrac{1}{8}(U_1^c+3U_2^c+U_3^c+3U_4^c),
\end{aligned}
\tag{2.19}
$$

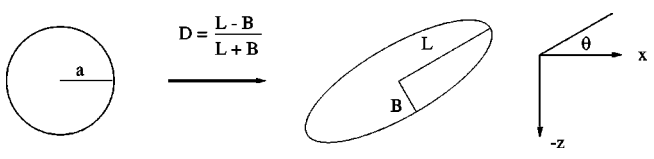

FIG. 4. Scalar measures of deformation and orientation.

TABLE I. Taylor deformation parameter D for steady-state drop for $\lambda=1$; Stokes flow. $\mathcal{A}$, $\mathcal{B}$ and $\mathcal{C}$ represent the computational domains $2\times1\times1$, $2\times1\times2$ and $2\times1\times4$, respectively.

Ca	0.10	0.15	0.20	0.25	0.30	0.35	0.40	0.42
$\mathcal{A}$						0.689	unsteady	unsteady
$\mathcal{B}$	0.119	0.181	0.244	0.309	0.372	0.469	0.585	unsteady
$\mathcal{C}$	0.114	0.172	0.232	0.293	0.360	0.436	0.541	

where the superscripts c, f denote coarse and fine grid values. The v-velocities can be prolongated by equivalent relations. To recover the concentration function on the coarse grid, the restriction procedure is simply made by averaging nearby values; that is

$$
\begin{aligned}
C^c(ic,jc)=\tfrac{1}{4}(&C^f(if,jf)+C^f(if+1,jf)+C^f(if,jf\\
&+1)+C^f(if+1,jf+1)).
\end{aligned}
\tag{2.20}
$$

This two-level method refines only the interface tracking on the finer grid and keeps the resolution of the velocity field on the coarse grid. This is a cheap way to improve accuracy, but it should be used with caution because the velocity [Eq. (2.19)] interpolated from the coarse grid is no longer divergence-free on the fine grid. This may violate the mass conservation. A divergence-free interpolation can be obtained through the following lower order formulas:

$$
\begin{aligned}
&U^f(if,jf)=U_1^c,\\
&U^f(if,jf+1)=U_1^c,\\
&U^f(if+1,jf)=U_1^c,\\
&U^f(if+1,jf+1)=U_1^c.
\end{aligned}
\tag{2.21}
$$

The direct simulation of two fluid flow is often limited by computing cost and machine memory, especially in the 3D case. Three issues have been of utmost importance in order to improve performance: The accuracy, the stability and the efficiency. The entire code has been parallelized: On the Origin2000 with 16 parallel processors, the efficiency of our code is more than 80%.

III. NUMERICAL STUDIES OF CRITICAL CAPILLARY NUMBER

In the simple shear flow illustrated in Fig. 1, the dynamics of the drop is essentially determined by two competing forces: the viscous shear stress $\mu_m\dot{\gamma}$ of the matrix liquid which causes the drop deformation and the characteristic Laplace pressure σ/a which resists the deformation. The capillary number $\mathrm{Ca}=\mu_m\dot{\gamma}a/\sigma$, defined as the ratio between

TABLE II. Orientation parameter $45-\theta$ of drop upon reaching steady state, for $\lambda=1$; Stokes flows. $\mathcal{A}$, $\mathcal{B}$ and $\mathcal{C}$ represent the computational domains $2\times1\times1$, $2\times1\times2$ and $2\times1\times4$, respectively.

Ca	0.10	0.15	0.20	0.25	0.30	0.35	0.40	0.42
$\mathcal{A}$						33.0	unsteady	unsteady
$\mathcal{B}$	8.48	12.1	15.0	17.1	19.6	25.3	30.7	unsteady
$\mathcal{C}$	8.58	12.3	15.5	17.9	19.1	23.3	27.3	

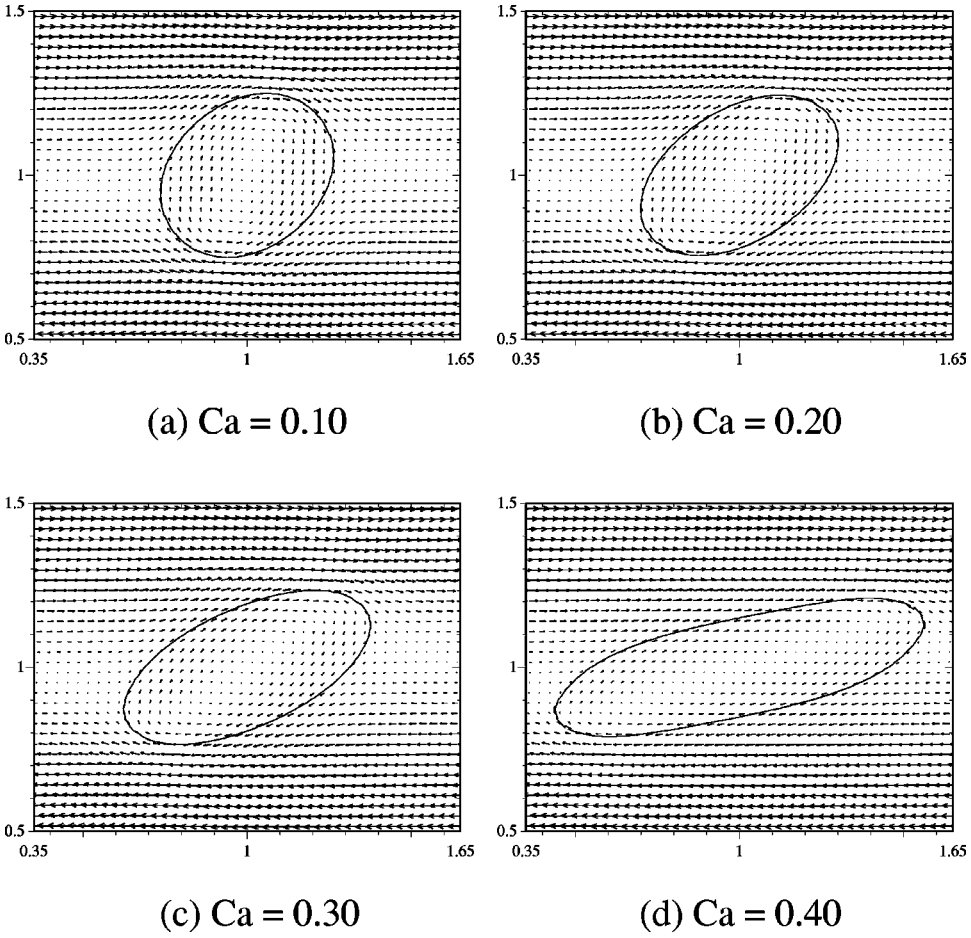

FIG. 5. Cross-sectional slice in the *x*-*z* plane through the center of the drop for steady-state solution in simple shear flow. $\lambda=1$, equal densities, Stokes flow. Velocity vectors are displayed.

these two forces, provides a useful measure of efficiency of the shear flow to deform the drop. Another important number is defined as the ratio of drop viscosity to matrix liquid viscosity $\lambda=\mu_d/\mu_m$. These two dimensionless parameters characterize the behavior of the suspended drop, provided the Reynolds number $\mathrm{Re}=\rho_m\dot{\gamma}a^2/\mu_m$ is small. Several previous experimental, theoretical and numerical studies have shown that when λ is less than four, there is a ''critical capillary number'' Ca_c, above which the drop continues to deform without reaching a steady shape, and this leads to disintegration. For capillary number Ca under the critical value, a steady drop shape exists in a steady shear flow. The critical capillary number for breakup of an isolated drop in shear flow is lowest for λ roughly around 0.6,[30] and the value is just slightly less than the case for $\lambda=1$, where $\mathrm{Ca}_c\approx 0.41$ is critical.[27]

In the case where the drop evolves to a steady shape, two parameters have been used to measure the deformation attained by the drop in its final stage. The first is the Taylor deformation parameter, $D=(L-B)/(L+B)$, where L and B are the half-length and half-breadth of the drop, respectively. The second parameter is the angle θ of orientation of the drop with the axis of shear strain (Fig. 4). Our first goal in this paper is to compute the critical capillary number accurately; i.e., for capillary number less than the critical value,

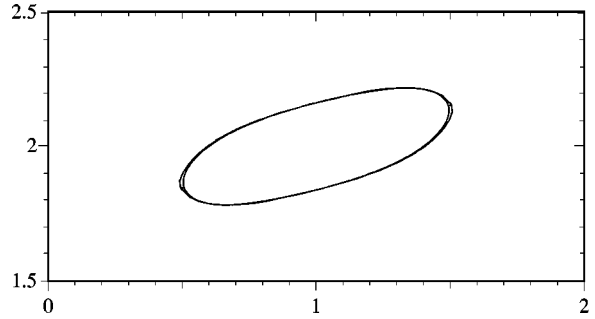

FIG. 6. Superposition of drop shapes obtained by one-level method (outer line) and two-level method (inner line). $2\times1\times4$ domain. $\mathrm{Ca}=0.40$, $\mathrm{Re}=0.0$, $\lambda=1$, equal densities. Cross-sectional slice in the *x*-*z* plane through the center of the drop.

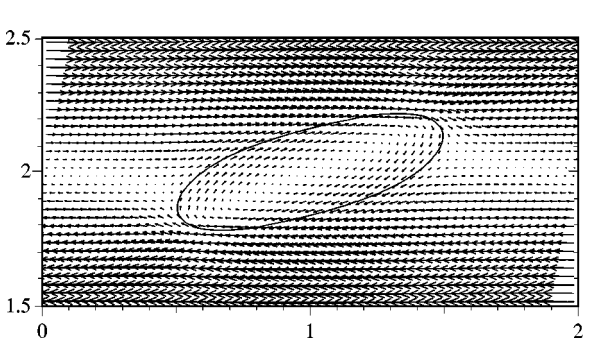

FIG. 7. Steady-state velocity field and drop shape for $\mathrm{Ca}=0.40$ calculated by the two-level method. $2\times1\times4$ domain, $\mathrm{Re}=0.0$, $\lambda=1$, equal densities. Cross-sectional slice in the *x*-*z* plane through the center of the drop.

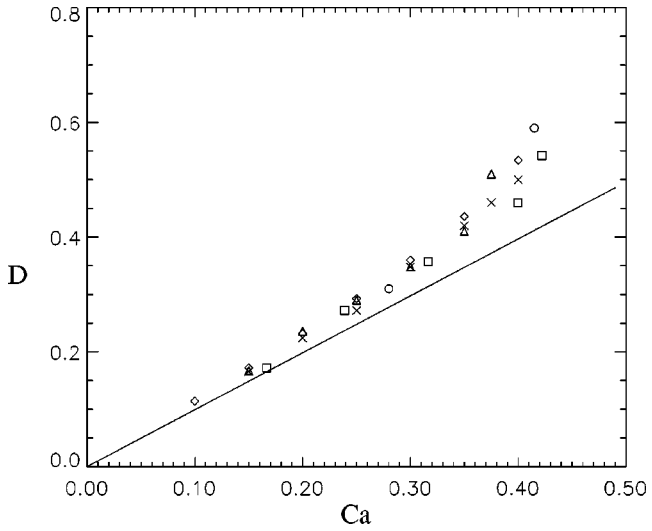

FIG. 8. Deformation of a viscous drop in simple shear flow. Comparison of the steady-state drop deformation parameter D for viscosity ratio $\lambda=1.0$, equal densities, Stokes flow. ◇ VOF computations; □ boundary integral computations of Rallison; × boundary integral computations of Kwak *et al.*; △ boundary integral computations of Kennedy *et al.*; ○ experimental results by Rumscheidt and Mason; the solid line represents the asymptotic results by Cox for small deformation (cf. Fig. 11 of Ref. 28).

we should obtain a steady solution. By comparing our results to the previous results in the literature, we can then judge the accuracy of the VOF method. We have studied the case which has been most analyzed in the literature with the boundary integral method: $\lambda=1$. The drop is given an initial radius $a=0.25$ and the unperturbed shear rate is 1.0. The external Reynolds number is then $\mathrm{Re}=\rho_e\dot{\gamma}a^2/\mu_e=0.0625$, and this is in the Stokes flow regime. For Ca less than the critical value, we have retrieved the same steady solution.

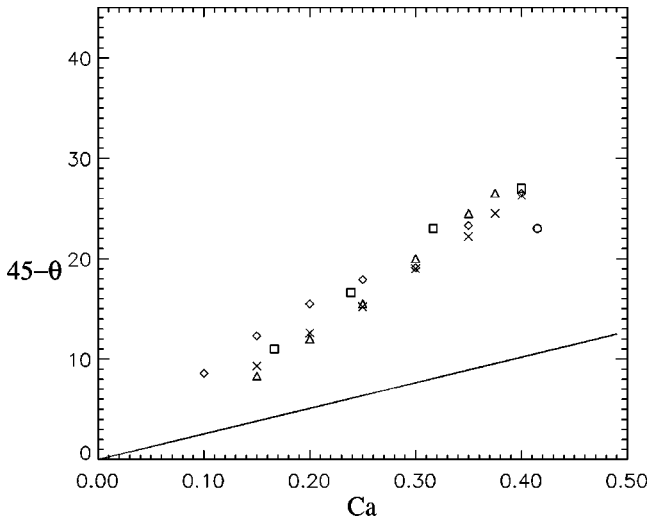

FIG. 9. Deformation of a viscous drop in simple shear flow. Comparison of the steady-state drop orientation angle θ measured in degree for viscosity $\lambda=1.0$, equal densities, Stokes flow. ◇ VOF computations; □ boundary integral computations of Rallison; × boundary integral computations of Kwak *et al.*; △ boundary integral computations of Kennedy *et al.*; ○ experimental results by Rumscheidt and Mason; the solid line represents the asymptotic results by Cox for small deformation (cf. Fig. 11 of Ref. 28).

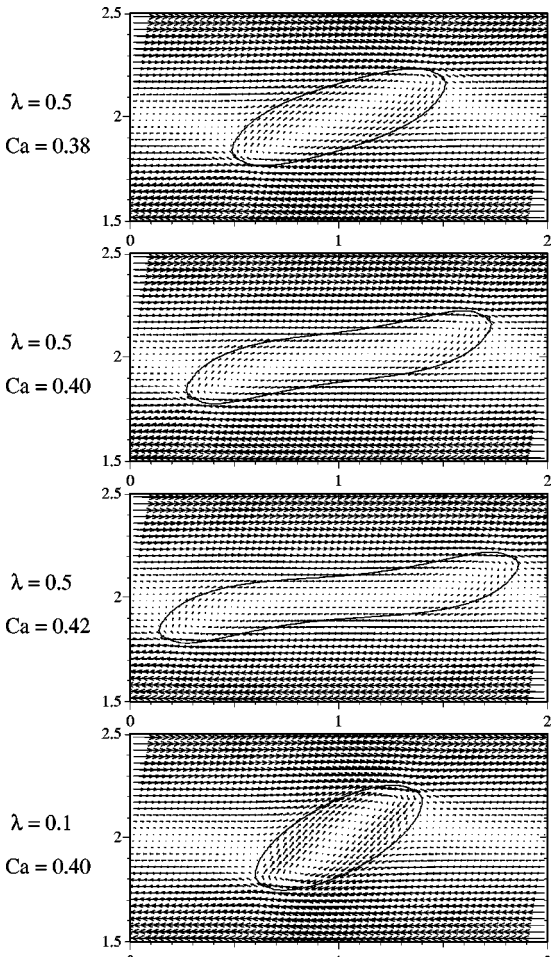

FIG. 10. Cross-sectional slice in x-z plane through the center of the drop. In the top three figures, the viscosity ratio is $\lambda=0.5$ and $\mathrm{Ca}=0.38$, 0.40, 0.42. In the bottom plot, $\lambda=0.1$, $\mathrm{Ca}=0.40$. The top and bottom solutions have achieved steady states. Equal densities, Stokes flow.

Numerical simulations of Stokes flows have been conducted for capillary numbers $\mathrm{Ca}=0.10$, 0.15, 0.20, 0.25, 0.30, 0.35, 0.40, and 0.42. The computational domains are boxes of dimensions $2\times1\times1$, $2\times1\times2$, and $2\times1\times4$. The difference in height among the boxes is used to investigate the effect of plate separation. The initial condition at time $T=0.0$ is that the drop has a spherical form and the initial velocity field is null inside the computational domain. The no-slip condition is imposed on the top and bottom plates and periodic conditions in the x direction and y direction. Constant velocities are imposed on the top and bottom plates such that the shear rate is constant during the whole computation. All the computations have been done with the one-level method. The mesh sizes are $\Delta x=\Delta y=\Delta z=1/32$. The parameters D and θ for the steady-state solutions are shown in Tables I and II, respectively.

The first remark from these computations is that the VOF method is accurate and we are able to predict the correct critical capillary number. In the $2\times1\times2$ computational domain, we obtained a steady solution for capillary number $\mathrm{Ca}=0.40$ and the flow is unsteady for $\mathrm{Ca}=0.42$. This result agrees with previous numerical results obtained with boundary integral methods. Figure 5 shows cross sections of the

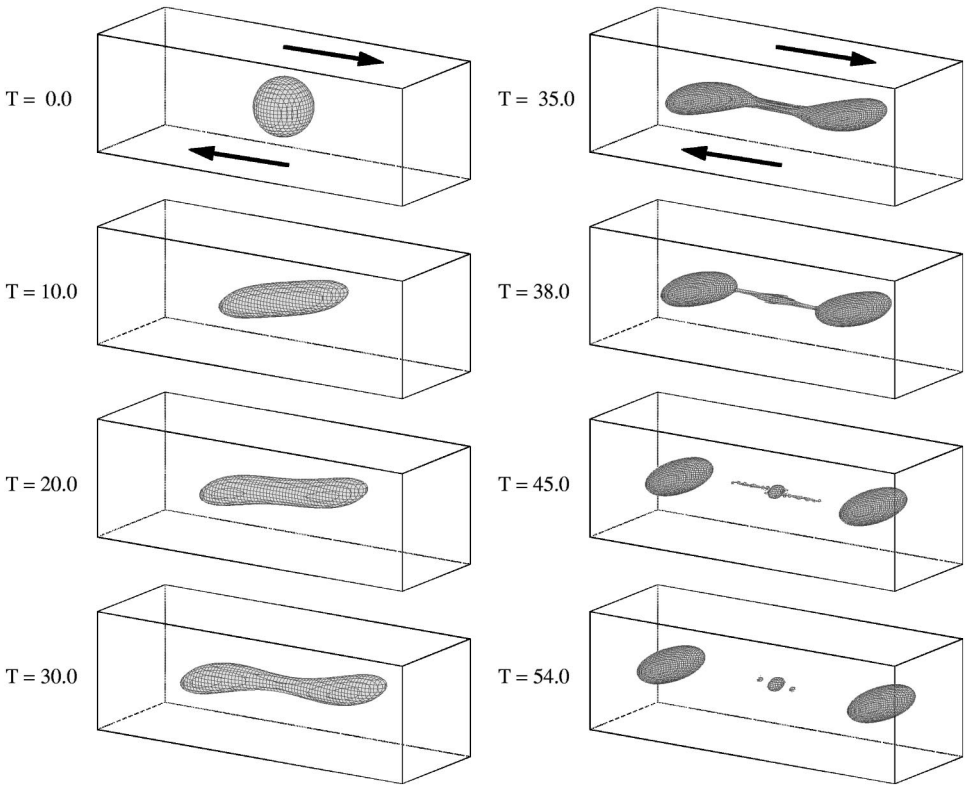

FIG. 11. Evolution of drop shape for Ca=0.42 in domain $3\times1\times2$, $\lambda=1$, equal densities, Re=0.0.

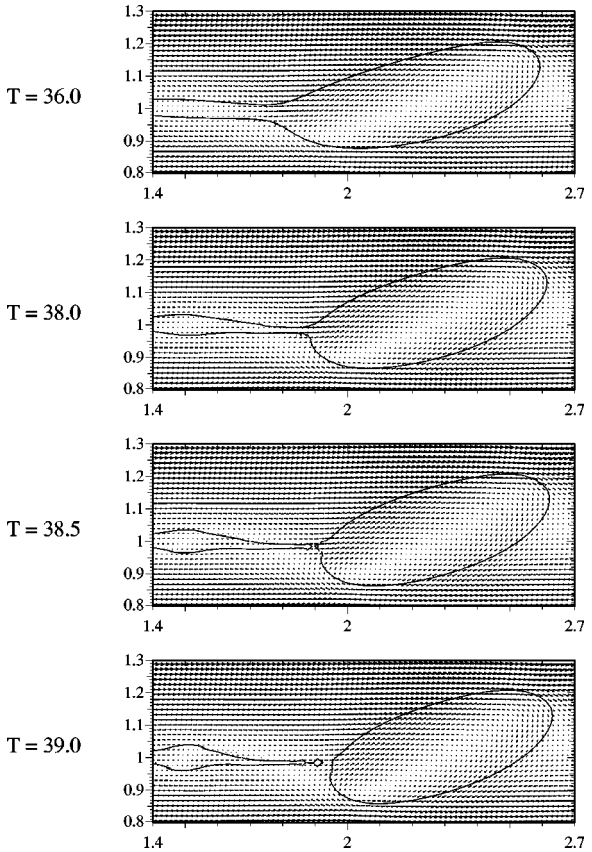

FIG. 12. Cross-sectional slice in the *x*-*z* plane through the center of the drop. Velocity vector fields in the *x*-*z* plane are shown during the breakup of a drop in simple shear flow for capillary number Ca=0.42, $\lambda=1$, equal densities, Re=0.0.

steady shapes in the *x*-*z* plane for Ca=0.1, 0.2, 0.30, and 0.40. It is evident that the larger the capillary number, the larger the drop deformation and rotation. We should mention that mass conservation is essential for the accurate calculation of the steady parameters D and θ. If a method were to lose mass during the calculation, the effective capillary number would decrease and the method would overestimate the surface tension force. Our simulations show that our VOF method has a very accurate mass conservation property. For example, take the Ca=0.40 case; the total VOF of the drop is 2144.675 initially, and it is 2144.619 when the steady solution is reached. The loss of mass is 0.0026%. This level of precision is yet to be achieved by the front-tracking and level set methods.

Secondly, we study the influence of the distance between the two plates where the boundary conditions are imposed. In all these calculations, the undeformed drop has radius $a=0.25$. When the plate separation is small ($d=1$ or $d/a=4$), no steady solution was obtained for Ca=0.40. The close proximity of the two plates reduces the critical capillary number. On the other hand, for large plate separations ($d=2$, 4, or $d/a=8$, 16), the liquids have more space to arrange themselves and the results show less sensitivity to the placement of the walls. The effect of Reynolds number was also studied by investigating the Navier–Stokes flow at the previously mentioned Re=0.0625. On the computational domain $2\times1\times2$, we obtained the steady parameters $D=0.312$ and $\theta=28.1$ for Ca=0.25. These values are only slightly larger than the values obtained from Stokes flow. We

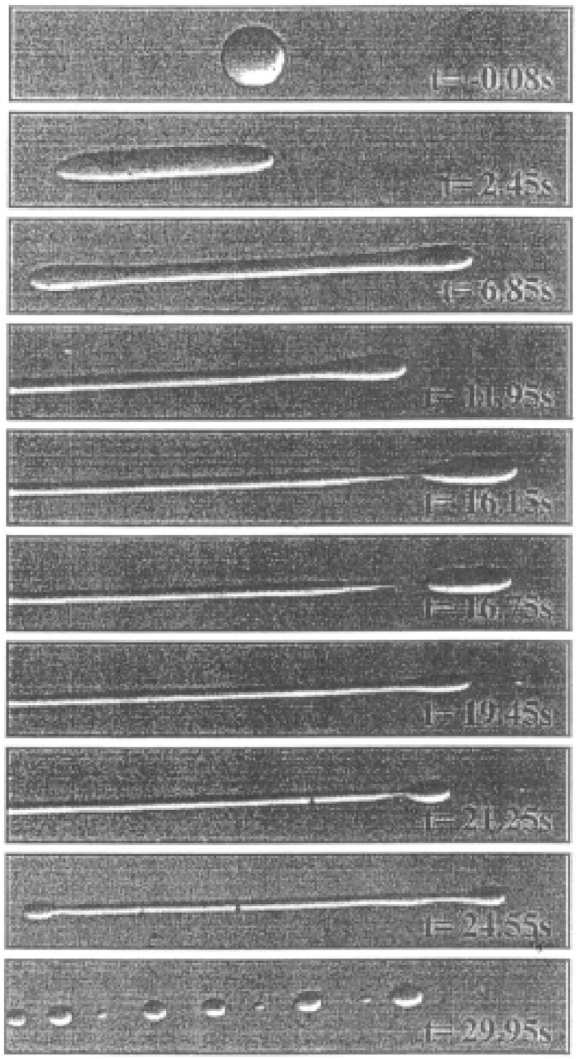

FIG. 13. Reproduction of Fig. 4.3.1.a of Ref. 5 showing a typical breakup. Matrix viscosity 7.0 Pa.s, drop viscosity 4.3 Pa.s, interfacial tension 10.7 mN/m, initial drop radius 0.048 cm, shear rate 2.17/s, equal densities.

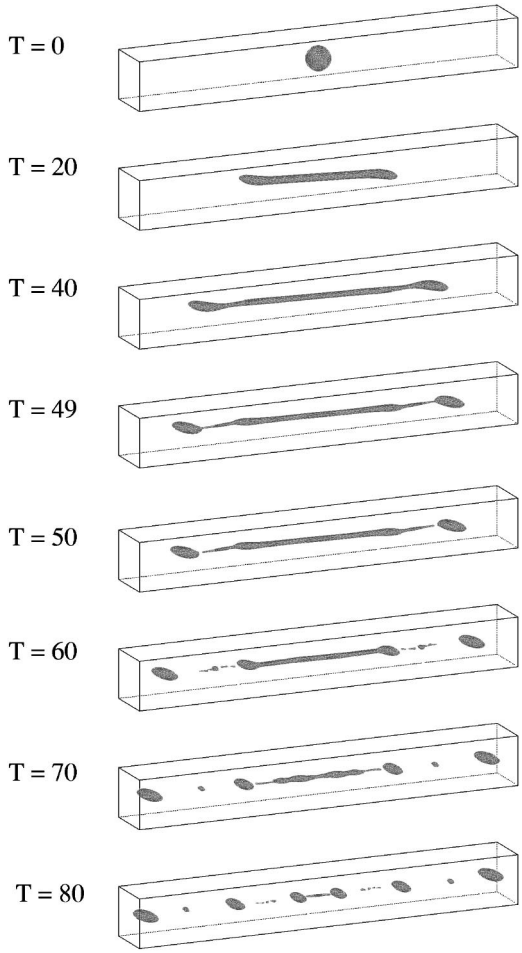

FIG. 14. Interface evolution as viewed from the side of the computational box $8\times1\times1$ during breakup for Ca$=0.45$, Re$=0.125$, $\lambda=1$, equal densities. $256\times64\times64$ grid.

conclude that the unsteady Stokes flow is a good approximation for low Reynolds number flow.

Our steady parameters obtained from the $2\times1\times4$ domain agree well with those of Refs. 28 and 29 which treat the case of walls out at infinity, for small capillary numbers. For example, for Ca$=0.20$, we obtained $D=0.232$, while $D=0.224$ in Ref. 28 and $D=0.236$ in Ref. 29. For Ca$=0.25$, we obtained $D=0.293$, while $D=0.272$ in Ref. 28 and $D=0.290$ in Ref. 29. However, the discrepancy widens for larger capillary number. We obtained $D=0.541$ for Ca$=0.40$, in comparison to $D=0.50$ in Ref. 28 and no steady solution is found in Ref. 29. We believe that this is essentially due to the lack of mesh refinement. The larger the capillary number, the more the drop is stretched, and the larger the curvature at the ends of the drop. Hence, more resolution is needed for accurate computation of the surface tension force. To justify this idea, we have refined the representation of the interface on the $2\times1\times4$ domain. For reason of efficiency, we used the two-level method rather than refining the entire mesh. We obtained the improved result of $D=0.534$ and $\theta=18.5$. The significance of this is shown in Fig. 6, where the drop shapes obtained by the two-level and the one-level methods are superimposed; the inner line is computed with the two-level method and the outer line with the one-level method. The two drop shapes coincide well except at the ends, where the curvature is large. Therefore, the results obtained by the two-level method represent a significant improvement on those by the one-level method.

To examine more carefully the drop deformation in the shear flow, we plot the drop shape and the velocity fields in the x-z plane, cut through the middle of the bubble, in Fig. 7. This provides a very nice visualization of the flow pattern of the drop in shear flow. Far away from the droplet, we see the basic simple shear flow pattern, with the flow moving toward the left at the top and toward the right at the bottom. Near the droplet, the velocity is tangential to the interface and the flow moves along the interface, which is consistent with the conditions at a free surface. The competition between the externally imposed shear flow and the surface tension driven flow produces a closed vortical motion interior to the drop.

Figures 8 and 9 show graphs of D and θ for the steady states attained for viscosity ratio $\lambda=1$, along with results of previous experimental and numerical investigations (cf. Fig. 11 of Ref. 28). We conclude that the VOF method obtains results comparable to the boundary integral method.

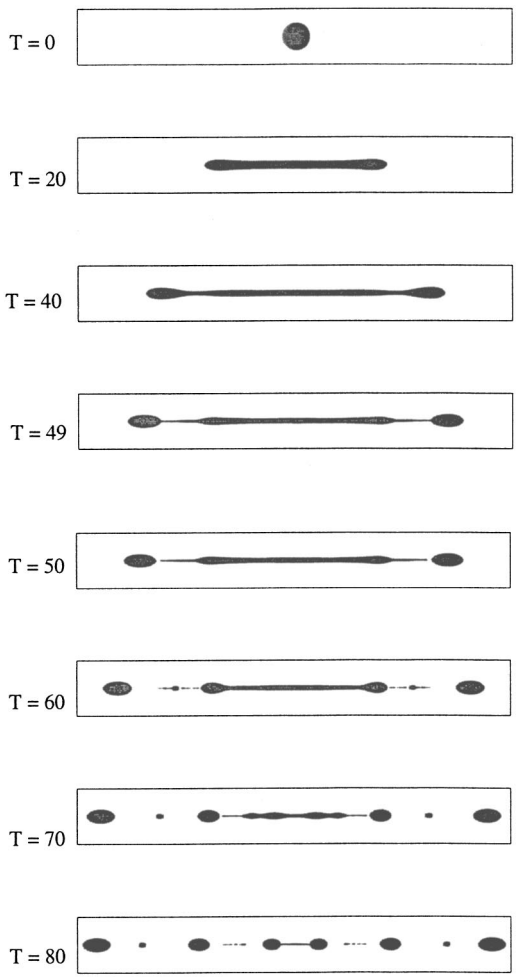

FIG. 15. Interface evolution as viewed from the top of the computational box $8\times1\times1$ during breakup for Ca=0.45, Re=0.125, $\lambda=1$, equal densities. $256\times64\times64$ grid.

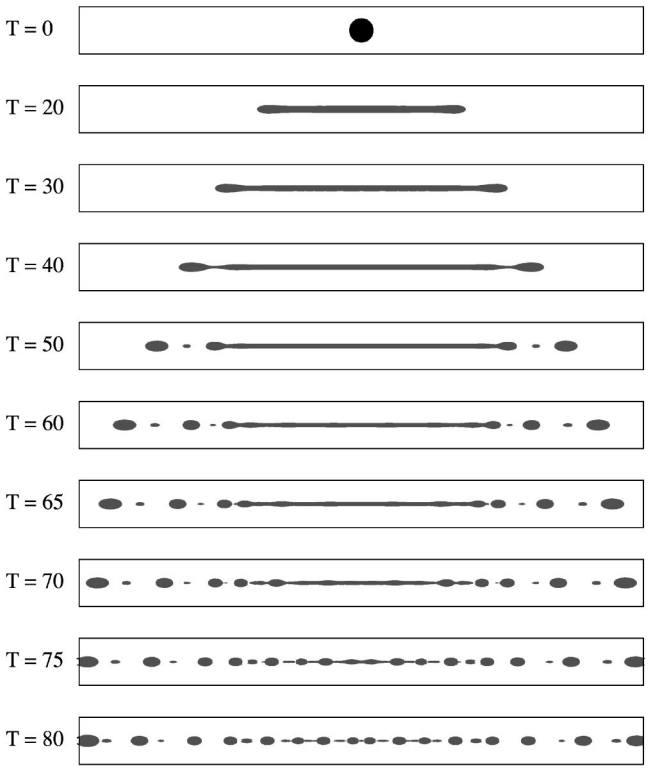

FIG. 16. Interface evolution as viewed from the top of the computational box $12\times1\times1$ during breakup for Ca=0.55, $\lambda=0.77$, equal densities. $256\times64\times64$ grid.

We have also investigated the critical capillary number for different viscosity ratios λ. The top three plots in Fig. 10 show the case $\lambda=0.5$ and the bottom plot shows the case $\lambda=0.1$, with equal densities, and zero Reynolds number. The sequence of shapes for $\lambda=0.5$ are the solutions after a relatively long time for Ca=0.38, 0.40, and 0.42. The elliptical shape for Ca=0.38 is attained as a steady-state solution. The Taylor parameter is $D=0.55$. The shapes for Ca=0.40 and 0.42 are still evolving toward the dumbbell shape. The evolution for Ca=0.40 is extremely slow, indicating that this capillary number is close to and above the critical value for breakup. Both Ca=0.40 and 0.42 clearly display the formation of the waist near the center of the drop, which signals the initiation of breakup. Our simulations show that the critical capillary number for viscosity ratio $\lambda=0.5$ lies between 0.38 and 0.40, which is slightly less than the one for $\lambda=1$. This is in good agrement with Grace's experimental data,[30] for which the minimum critical capillary number is in the region of $\lambda=0.6$, and is slightly less than that for $\lambda=1$. Their data show also that at viscosity ratios much less than 1, or much greater than 1, the critical capillary number increases rapidly. We have also confirmed this. The bottom plot in Fig. 10 shows the steady-state shape for $\lambda=0.1$ and Ca=0.40. The drop has an ellipsoidal form and the Taylor parameter is $D=0.44$, which is much less than the $D=0.54$ for $\lambda=1$. This confirms that a much larger critical capillary number is needed for drop breakup at this low viscosity ratio. The velocity vector plot clearly shows that the vortical motion inside the drop is markedly stronger than for $\lambda=1$ because the drop liquid is now much less viscous than the matrix liquid.

IV. RUPTURING A DROP IN SHEAR WITH THE VOF CODE

When the shear rate is increased past a critical value, the drop ruptures. Based upon previous works, the critical capillary number for $\lambda=1$ is roughly 0.41. Indeed, our computation predicts an unsteady solution for Ca=0.42 in the domain $3\times1\times2$. Figure 11 shows the evolution of the drop shape on a $96\times32\times64$ mesh grid. The drop continuous to deform and eventually breaks up. The competition between the externally imposed shear flow and the surface tension driven flow is clearly evident in the figures. Initially, the most noticeable motion is the elongation of the drop, stretched by the viscous shear stress of the external flow (time T=0.0, 10.0, and 20.0). To time T=30.0, we see

TABLE III. Reynolds numbers just below break-up values for different capillary numbers. $\lambda=1$, equal densities.

Ca	0.1	0.15	0.2	0.25	0.3	0.35
Re	21.5	10.0	4.0	1.5	0.6	0.2

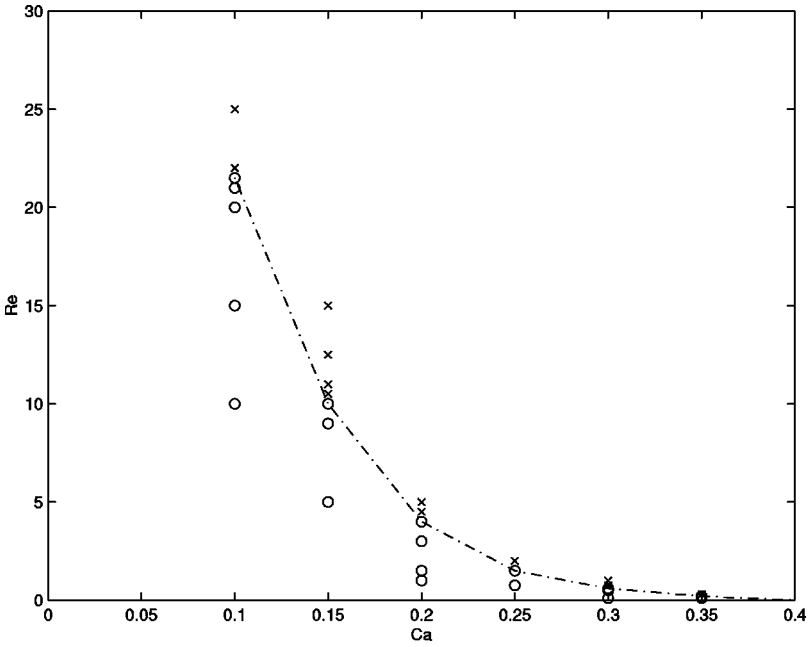

FIG. 17. Diagram of drop breakup in the (Ca,Re) plane. Circles represent evolution to steady state. Crosses represent breakup. Dashed curve interpolates critical values. $\lambda = 1$, equal densities.

clearly that a waist is formed near the center of the drop, and the drop continually thins. The drop is beginning to lengthen slowly and a visible neck is formed near the bulbous end. The subsequent scenario is described in Ref. 31; this neck will eventually lead to the ends pinching off and the remaining liquid thread in the middle will form some small satellite droplets. Moreover, the experimental work of Ref. 5 shows that there can be a sequence of large and small drops formed after the ends break off.

To examine more carefully the breakup procedure, we have done the calculation on a $192\times64\times128$ mesh-grid. We present the velocity field on the cross-sectional cut in the *x*-*z*

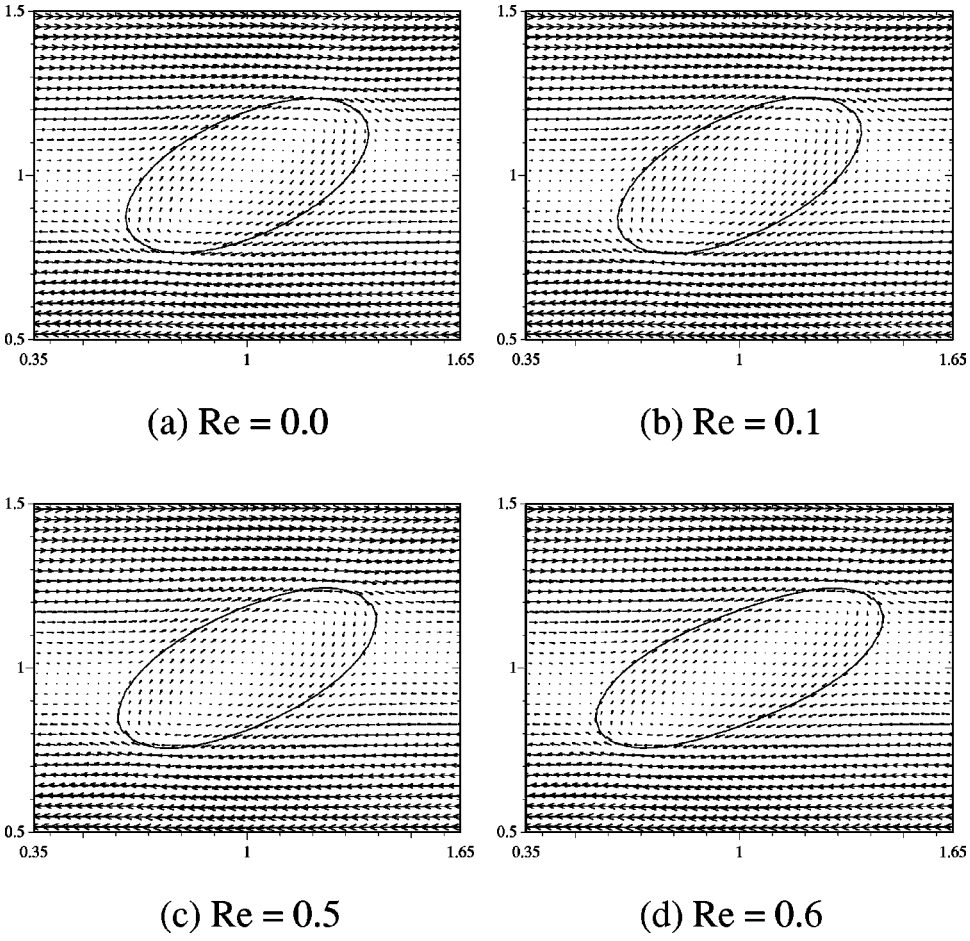

FIG. 18. Steady-state solutions for $\lambda = 1$, equal densities, and $Ca = 0.3$, for increasing Reynolds numbers (a) 0.0, (b) 0.1, (c) 0.5, (d) 0.6. The drop breaks up for Reynolds numbers just above 0.6. Velocity vector fields are shown for cross-sectional slices in the *x*-*z* plane.

TABLE IV. Variation of Taylor deformation parameter D with Reynolds number. $\lambda=1, Ca=0.3$, equal densities.

Re	0.0	0.1	0.5	0.6	0.75
D	0.372	0.3968	0.45	0.4768	break

plane in Fig. 12; the flow pattern is symmetrical and we need to show only the right half field. The precise role of the surface tension driven flow during breakup can be examined from this figure. At time T=36.0, the result of the competition between the external flow and the surface tension force is a vortical motion inside the bulbous end of the drop, except near the neck; the surface tension force drives a fast flow motion toward the bulbous end while in the waist near the center, the flow is much weaker. The consequence is that the neck quickly and continually narrows (the neck has the same size as the mesh grid at this time), while the width of the central waist remains almost unchanged at time T=38.0. At T=38.5, the drop breaks up at the neck and produces a main drop and a middle liquid thread.

For the simulation on the $192\times64\times128$ mesh-grid, we have used a time step $\Delta t=5.0\times10^{-3}$, and the Neumann number is 2, eight times larger than the stable time step for the corresponding explicit method. Although our scheme is unconditionally stable for the viscous terms, we did not use larger time steps, in order to avoid an overshoot in the computations. This simulation required a total CPU time on ten Origin 2000 processors on the order of two weeks.

As noted by Ref. 5 in his Sec. IV F 2, the largest daughter drop formed during breakup is always formed by the first elongative end pinching. Our case of Ca=0.42, $\lambda=1$ is just above the critical capillary number, and the two main daughters contain almost all the volume of the initial drop; i.e., they are each ~0.5 of the initial volume. This would give an estimate of the radii to be $0.5^{1/3}=0.79$ of the initial drop radius. Indeed, the maximum daughter drop radius in the numerical simulation is slightly less at the third decimal place, rounding to $0.79a$, where a denotes the initial drop radius. In the notation of Ref. 5 where $\mathrm{Ca}_x=a_x\mu_m\gamma/\sigma$, a_x denotes the daughter radius, $K_x=\mathrm{Ca}_x/\mathrm{Ca}_c=0.8$, and $K_i=\mathrm{Ca}_i/\mathrm{Ca}_c=1.02$. Hence, our result is in agreement with his experimental result on maximum daughter drop size and comparison with a binary model, which is plotted in his Fig. 4.6.2.e.

Figure 13 reproduces Fig. 4.3.1.a of Ref. 5, which is an experimental observation of elongative end pinching. The drop is polybutadiene and the matrix liquid is a corn-syrup solution. The ratio of viscosities is $\lambda=0.61$ and the capillary number is Ca=0.68. The critical capillary number is stated as 0.48. This sequence of events is qualitatively similar to our results shown in Fig. 14 for the side-view and Fig. 15 for the top-view for $\lambda=1$ and Ca=0.45. The view from the top of the computational domain provides the analogy with the experimental pictures. The production of the largest drops at the ends, followed by a small, then large, then small, drops toward the middle of the neck, is reproduced in our computations. Figure 13 is described at length in Ref. 5 and we summarize it here: ''As the drop stretches, it first takes on an

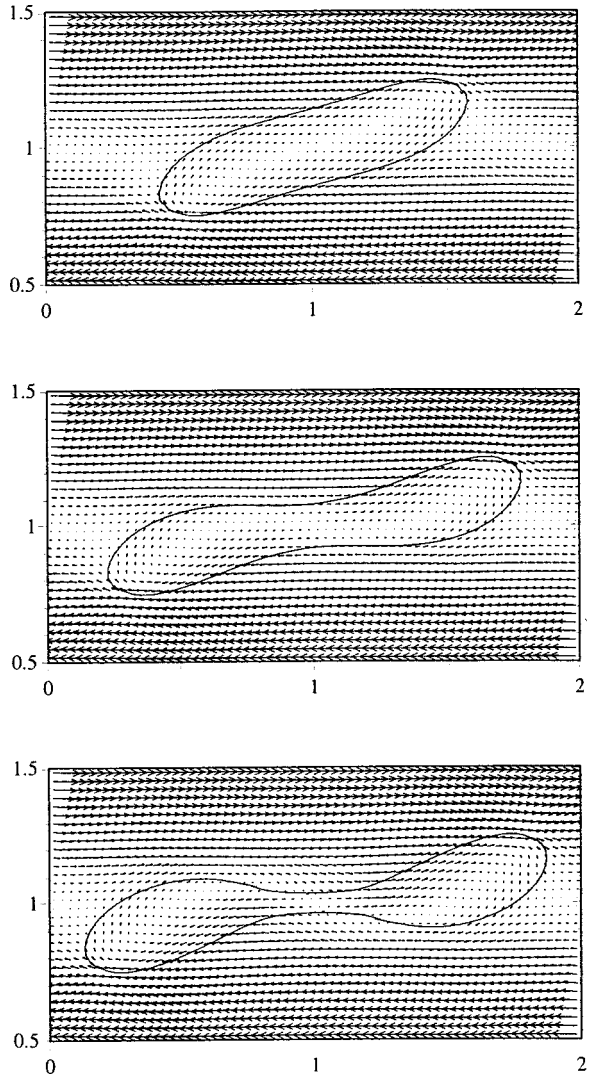

FIG. 19. A sequence of deformation leading to breakup of drop for $\lambda=1$, equal densities, Ca=0.3, and Reynolds number 0.75. Cross-sectional slice in the x-z plane through the center of the drop.

ellipsoid shape. At some point, time about 2.45 s'' in Fig. 13, ''the drop changes from an ellipsoid shape to a 'dumbbell' shape similar to that observed in retractive end pinching. The drop continues to stretch. The 'bulbs' at the end of the drop achieve a stable diameter. The center portion of the drop continues to thin. Eventually, a bridge develops between the center portion of the drop (time about 11.95 s in Fig. 13). This bridge is unstable and leads to the bulb pinching off to form a new drop (time about 16.75 s in Fig. 13). If the drop is large enough (i.e., if the original volume is not totally used up by the formation of the first bulb drops) the ends of the center portion will ''bulb up'' in a process similar to retractive end pinching. A bridge will form between this subsequent bulb and the center portion of the drop and a second bulb drop will break off.'' The experimental observations of breakup all ''began with a breakup of the elongative end pinching type. Subsequent end pinches and capillary wave breakups were observed only when the shear rate exceeded the critical shear rate by a sufficient amount.''

Figure 16 shows our numerical computation for viscos-

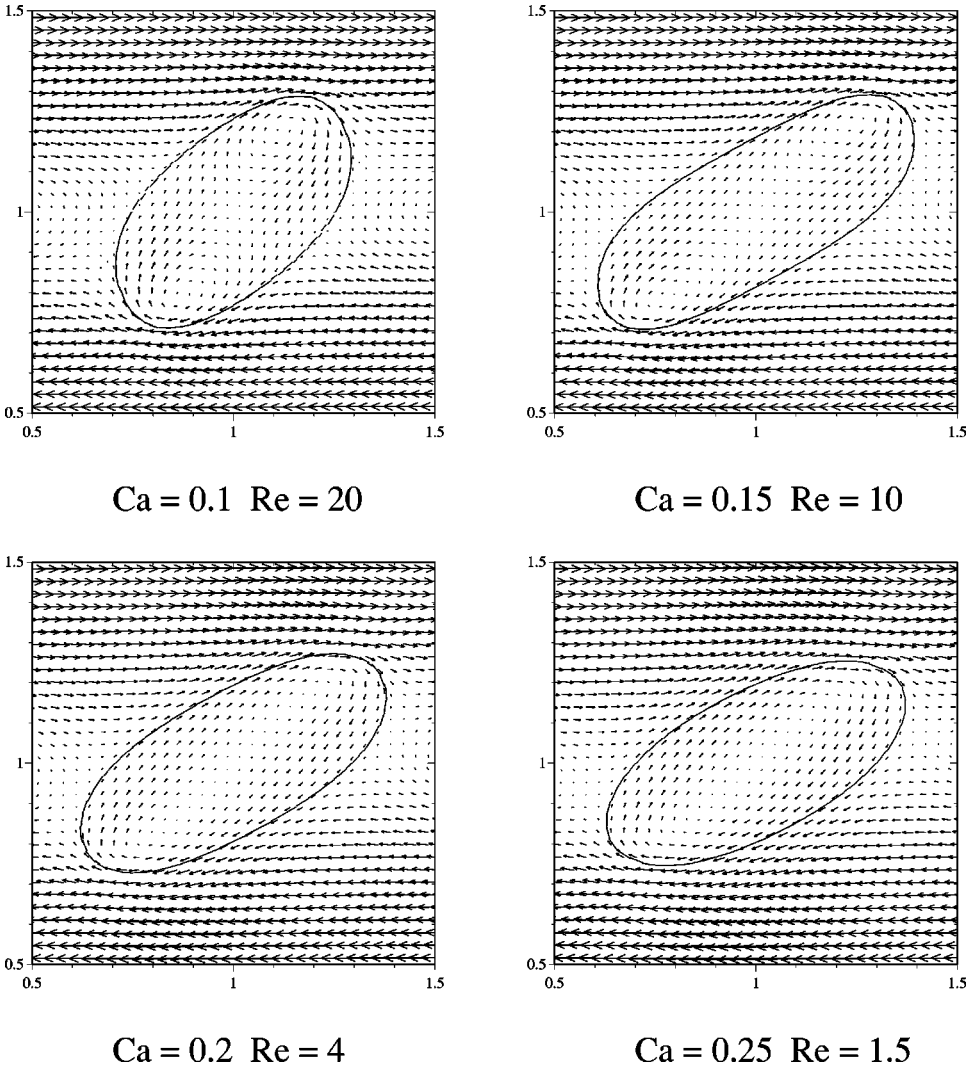

FIG. 20. Steady-state solutions at different capillary numbers for Reynolds numbers just below break-up values. $\lambda = 1$, equal densities. Cross-sectional slice in the *x*-*z* plane through the center of the drop.

ity ratio $\lambda = 0.77$ and $\mathrm{Ca} = 0.55$, with equal densities. These parameters are closer to those of Fig. 13; the dynamics are again similar to that of Fig. 15 for $\lambda = 1$, $\mathrm{Ca} = 0.45$. The drop stretches from spheroidal to ellipsoidal then to the dumbbell shape, the ends pinch off, producing the largest daughter drops, followed by instabilities of the central portion, producing small and large drops. Note that Fig. 16 even agrees with the experimental picture in Fig. 13 in the production of the primary large drop followed by a small drop, then a large drop, then a small drop, then two large drops toward the center of the neck.

V. EFFECT OF THE REYNOLDS NUMBER

In this section, we focus on the case $\lambda = 1$, as the Reynolds number is increased. Our computational domain is a box of dimensions $2 \times 1 \times 2$, with a mesh of $64 \times 32 \times 64$. As we saw before, the placement of the walls has a minor effect and the mesh is sufficient to produce quantitatively accurate results. For zero Reynolds number, the case $\lambda = 1$ and equal densities has a critical capillary number of 0.41. For capillary numbers below this value, Table III shows that breakup is induced when the Reynolds number is increased past a critical value. The critical Reynolds number is small for Ca close to 0.4, but increases rapidly as Ca decreases. This trend is shown in Fig. 17, where the horizontal axis represents the capillary numbers up to 0.4, and the vertical axis is the Reynolds number. Computations were performed at a number of points on this plot. The circles represent our numerical calculations which yield steady-state solutions, and the crosses yield breakup. The dashed curve represents critical values.

At each capillary number, the increase in Reynolds number deforms the drop from ellipsoidal to elongated. This is illustrated for $\mathrm{Ca} = 0.3$ in Fig. 18. In comparison with the velocity fields for Stokes flow shown in Fig. 5, the increase in Re leads to a markedly stronger velocity field in the drop region. For example, Fig. 18(d) shows the strong vortical motion inside the drop just below the critical Reynolds number. Table IV shows the accompanying increase in the Taylor deformation parameter D for the steady-state solution, as the Reynolds number is increased.

Figure 19 shows the evolution of the drop toward breakup for $\mathrm{Ca} = 0.3$ at $\mathrm{Re} = 0.75$. The shapes here are analogous to the sequence shown in Fig. 11 for the case of equal viscosities, since the critical Reynolds number is still low.

Figure 20 shows the steady-state solutions for capillary numbers 0.1, 0.15, 0.2, and 0.25 just below the critical Rey-

nolds numbers. At each capillary number, the spherical drop evolves to a steady solution up to roughly the value shown in this figure. This figure shows that increasing the Reynolds number leads to two effects. First, the symmetry across the mid-plane of the steady state is lost, and it loses its ellipsoidal shape. For the lower capillary numbers, the drop is more vertically inclined than in the case of the higher capillary numbers. Secondly, the flowfield inside the drop develops more than one vortex. Two vortices are clearly visible for $Ca=0.1$, $Re=20$, and $Ca=0.15$, $Re=10$. The lower the capillary number, the stronger the interfacial tension which keeps the drop together, and the higher the Reynolds number that is required to break up the drop. At the higher Reynolds numbers, the velocity fields show the distinct development of more complicated dynamics in the drop region.

VI. CONCLUSION

A VOF method has been used to investigate the deformation and breakup of a drop in simple shear flow. The critical capillary number for breakup, the Taylor deformation parameter D, and angle of orientation, have been checked against previous works, including the experimental work of Ref. 30 for viscosity ratios different from one. For low capillary numbers where drop breakup does not occur in Stokes flow, we have induced breakup with an increased Reynolds number. The main advantage of our method is its mass conservation property, so that no rescaling of the mass is needed during the calculation. Another advantage of the VOF method lies in its ability to compute flows with changes in topology. We have investigated the breakup of a drop for supercritical capillary numbers and examined the end pinching mechanism. The capability of the VOF method to study the drop dynamics beyond the steady state is confirmed with comparisons on the details of the daughter drops with the experimental data of Ref. 5.

ACKNOWLEDGMENTS

We thank Costas Pozrikidis and Sehoon Kwak for giving us their data for Figs. 8 and 9. We thank Richard V. Calabrese for discussions and for making available to us the PhD thesis of Charles R. Marks. We thank Gareth McKinley, Vittorio Cristini, Michael Loewenberg, and Howard Stone for discussions. This research was sponsored by the National Science Foundation under Grant Nos. CTS-9612308 and DMS-9870220.

[1]G. I. Taylor, ''The viscosity of a fluid containing small drops of another fluid,'' Proc. R. Soc. London, Ser. A **138**, 41 (1932).
[2]G. I. Taylor, ''The formation of emulsions in definable fields of flow,'' Proc. R. Soc. London, Ser. A **146**, 501 (1934).
[3]J. M. Rallison, ''The deformation of small viscous drops and bubbles in the shear flows,'' Annu. Rev. Fluid Mech. **16**, 45 (1984).
[4]H. A. Stone, ''Dynamics of drop deformation and breakup in viscous fluids,'' Annu. Rev. Fluid Mech. **26**, 65 (1994).
[5]C. R. Marks, ''Drop breakup and deformation in sudden onset strong flows,'' Ph.D. thesis, University of Maryland at College Park, 1998.
[6]B. J. Bentley and L. G. Leal, ''An experimental investigation of drop deformation and breakup in steady, two-dimensional linear flows,'' J. Fluid Mech. **167**, 241 (1986).
[7]T. G. Mason and J. Bibette, ''Shear rupturing of droplets in complex fluids,'' Langmuir **13**, 4600 (1997).
[8]M. Siegel, ''Influence of surfactant on rounded and pointed bubbles in two-dimensional Stokes flow,'' SIAM J. Appl. Math. **59**, 1998 (1999).
[9]M. Loewenberg and E. J. Hinch, ''Numerical simulation of a concentrated emulsion in shear flow,'' J. Fluid Mech. **321**, 395 (1996).
[10]V. Cristini, J. Blawzdziewicz, and M. Loewenberg, ''Drop breakup in three-dimensional viscous flows,'' Phys. Fluids **10**, 1781 (1998).
[11]J. Li, Y. Renardy, and M. Renardy, ''A numerical study of periodic disturbances on two-layer Couette flow,'' Phys. Fluids **10**, 3056 (1998).
[12]J. Li and Y. Renardy, ''Direct simulation of unsteady axisymmetric core-annular flow with high viscosity ratio,'' J. Fluid Mech. **391**, 123 (1999).
[13]R. Scardovelli and S. Zaleski, ''Direct numerical simulation of free surface and interfacial flow,'' Annu. Rev. Fluid Mech. **31**, 567 (1999).
[14]R. DeBar, ''Fundamentals of the KRAKEN Code,'' *Technical Report UCIR-760, LLNL*, 1974.
[15]D. L. Youngs, ''Time-dependent multi-material flow with large fluid distortion,'' in *Numerical Methods for Fluid Dynamics* (Academic, New York, 1982), p. 27.
[16]J. Li, ''Calcul d'Interface Affine par Morceaux (Piecewise Linear Interface Calculation),'' C. R. Acad. Sci. Paris, **t.320 série IIb**, 391 (1995).
[17]J. Li, ''Numerical resolution of Navier-Stokes equation with reconnection of interfaces. Volume tracking and application to atomization,'' Ph.D. thesis, University of Paris VI, 1996.
[18]E. J. Puckett, A. S. Almgren, J. B. Bell, D. L. Marcus, and W. J. Rider, ''A second-order projection method for tracking fluid interfaces in variable density incompressible flows,'' J. Comput. Phys. **130**, 269 (1997).
[19]W. J. Rider and D. B. Kothe, ''Reconstructing volume tracking,'' J. Comput. Phys. **141**, 112 (1998).
[20]S. Popinet and S. Zaleski, ''A front-tracking algorithm for the accurate representation of surface tension,'' Int. J. Numer. Methods Fluids **30**, 775 (1999).
[21]B. Lafaurie, C. Nardone, R. Scardovelli, S. Zaleski, and G. Zanetti, ''Modelling merging and fragmentation in multiphase flows with SURFER,'' J. Comput. Phys. **113**, 134 (1994).
[22]A. V. Coward, Y. Renardy, M. Renardy, and J. R. Richards, ''Temporal evolution of periodic disturbances in two-layer Couette flow,'' J. Comput. Phys. **132**, 346 (1997).
[23]D. Gueyffier, J. Li, A. Nadim, R. Scardovell, and S. Zaleski, ''Volume-of-fluid interface tracking and smoothed surface stress methods applied to multiphase flow and pendant drop pinching,'' J. Comput. Phys. **152**, 423 (1999).
[24]J. U. Brackbill, D. B. Kothe, and C. Zemach, ''A continuum method for modeling surface tension,'' J. Comput. Phys. **100**, 335 (1992).
[25]A. J. Chorin, ''A numerical method for solving incompressible viscous flow problems,'' J. Comput. Phys. **2**, 12 (1967).
[26]A. Brandt, ''Multi-level adaptive solutions to boundary-value problems,'' Math. Comput. **31**, 333 (1977).
[27]J. M. Rallison, ''A numerical study of the deformation and burst of a drop in general shear flows,'' J. Fluid Mech. **109**, 465 (1981).
[28]S. Kwak and C. Pozrikidis, ''Adaptive triangulation of evolving closed, or open surfaces by the advancing-front method,'' J. Comput. Phys. **145**, 61 (1998).
[29]M. R. Kennedy, C. Pozrikidis, and R. Skalak, ''Motion and deformation of liquid drops and the rheology of dilute emulsions in simple flow,'' Comput. Fluids **23**, 251 (1994).
[30]H. P. Grace, ''Dispersion phenomena in high viscosity immiscible fluid systems and application of static mixers as dispersion devices in such systems,'' Chem. Eng. Commun. **14**, 225 (1982).
[31]H. A. Stone, B. J. Bentley, and L. G. Leal, ''An experimental study of transient effects in the breakup of viscous drops,'' J. Fluid Mech. **173**, 131 (1986).